

# Pygmy resonance and torus mode within Vlasov dynamics

Michael Urban

*Institut de Physique Nucléaire, CNRS-IN2P3 and Université Paris-Sud 11, 91406 Orsay cedex, France*

The pygmy dipole resonance in neutron-rich nuclei is studied within the framework of the Vlasov equation which is solved numerically. The interaction used in the Thomas-Fermi ground state and in the Vlasov equation is derived from an energy functional which correctly describes the equation of state of nuclear matter and neutron matter. It is found that the pygmy resonance appears in the electric dipole response of all nuclei with strong neutron excess, the energies and transition probabilities being in reasonable agreement with experimental results. Since the Vlasov equation does not account for any shell effects, this indicates that the existence of the pygmy resonance is a generic phenomenon and does not rely on the specific shell structure. Besides the electric dipole response, the isoscalar toroidal response is calculated. The transition densities and velocity fields are discussed. A comparison of the peak positions and velocity fields suggests that the pygmy resonance can be identified with one of the low-lying modes excited by the isoscalar toroidal operator.

PACS numbers: 21.10.Re, 24.30.Cz, 03.65.Sq, 02.70.Ns

## I. INTRODUCTION

Neutron rich nuclei have become a very popular object of experimental and theoretical nuclear structure studies. Besides the crucial role these nuclei play in nuclear astrophysics and their importance for constraining the nuclear energy density functional, these nuclei exhibit fascinating properties which are qualitatively different from ordinary nuclei. For instance, as a consequence of the “neutron skin” surrounding the core of medium-mass and heavy neutron-rich nuclei, there are new kinds of collective motion which are absent in nuclei without strong neutron excess (see [1] for a recent review).

A famous example for such a collective mode is the so-called pygmy resonance. Contrary to the well-known isovector giant-dipole resonance (GDR), where neutrons and protons move against each other, the pygmy-dipole resonance (PDR) consists, roughly speaking, of an oscillation of the neutron skin against the  $N = Z$  core. This mode is not only interesting in itself, but its existence has also a strong effect on the abundances of the elements in the universe [2]. After first studies within schematic hydrodynamic models [3, 4], the pygmy mode was investigated within the random-phase approximation (RPA), using non-relativistic [5] or relativistic formalisms [6, 7], and beyond, using the quasiparticle-phonon model [8, 9].

Another exotic type of collective motion is the “toroidal dipole mode”. This isoscalar mode, which is characterized by a velocity field of toroidal shape, was predicted many years ago [10]. Since the restoring force for this kind of motion is generated by the distortion of the Fermi surface, this mode cannot be described within hydrodynamic models. Studies of this mode were carried out within the method of Wigner function moments [11], within nuclear fluid dynamics [12], and within the relativistic RPA [13]. Since the toroidal dipole mode is isoscalar and exists also in  $N = Z$  nuclei, it was usually not connected with the pygmy resonance, although different calculations [6, 8] showed that the velocity field of the pygmy mode has a toroidal shape.

In the past, semiclassical approaches such as the Steinwedel-Jensen model [14] contributed a lot to the understanding of giant resonances and how they can be related to global properties of nuclei. Since semiclassical approaches average over shell effects [15], they lead to clear and intuitive pictures which, contrary to the results of quantum mechanical RPA calculations, are not obscured by details of the specific single-particle energies and wave functions of the nuclei under consideration. This is why new modes of excitation, such as the torus mode mentioned before, were often first identified in semiclassical approaches.

In the case of the pygmy mode, a generally accepted picture is still missing. It is not even clear whether the pygmy mode is a generic collective mode like the giant resonances, or whether it depends on a particular structure of the single-particle levels. The aim of the present paper is therefore to study this mode by solving the semiclassical Vlasov equation for the case of neutron-rich nuclei. The Vlasov equation has been shown to give a reasonable description of generic properties of different collective modes of nuclei [16–18]. As we will see, the main result of the present study is that the pygmy mode is closely related to a low-lying isoscalar torus mode, which is clearly collective and whose existence is not limited to nuclei with neutron excess.

In this paper, we are looking for a numerical solution of the full Vlasov equation without any additional simplifying assumptions, as opposed to, e.g., fluid-dynamical approaches. A solution of the Vlasov equation for collective modes was given in Refs. [16, 17], but the calculations were restricted to Woods-Saxon potentials with separable residual interactions. This is not sufficient for the description of modes which possibly depend on exotic ground state properties such as the neutron skin. In the present work, the starting point is the ground state in Thomas-Fermi (TF) approximation, calculated self-consistently with the same interaction that is also used in the Vlasov dynamics. The importance of a consistent description of the ground state and of the dynamics

within a transport model was recently pointed out in Ref. [19] in the context of the monopole mode.

For the calculation of the mean field entering both the TF and the Vlasov calculations, an effective interaction capable of describing exotic nuclei is needed. In the present work, a simplified version of the so-called BCP functional [20] will be used, which is an energy functional whose bulk part is based on a fit to microscopic Brückner calculations, reproducing the equation of state of nuclear matter in a range of asymmetries from symmetric matter to pure neutron matter and in a range of densities from zero to more than saturation density. However, it seems unlikely that the general findings presented here depend on the details of the interaction.

The paper is organized as follows. In Sec. II, the method is explained. In Sec. III, results for the electric dipole response are presented. Besides the strength function, the transition densities and velocity fields of the GDR and the PDR are discussed. In Sec. IV, results for the response to the isoscalar toroidal dipole operator are shown. In particular, by comparing the transition densities and velocity fields with those discussed in Sec. III, we see that in neutron-rich nuclei, the PDR and the GDR are modes which are excited by both the electric dipole and the isoscalar toroidal dipole operators due to the mixing of isoscalar and isovector modes. Sec. V is devoted to the summary and conclusions.

## II. METHOD

### A. Vlasov equation

Like other collective vibrations, the pygmy resonance has been studied within the random-phase approximation (RPA) [5–7], which can be interpreted as the small-amplitude limit of the time-dependent Hartree-Fock (TDHF) theory [15]. Written in terms of the one-body density matrix  $\hat{\rho}$  and the mean-field hamiltonian  $\hat{h}$ , the TDHF equation reads<sup>1</sup>

$$i\hbar\dot{\hat{\rho}} = [\hat{h}, \hat{\rho}]. \quad (1)$$

In the semiclassical  $\hbar \rightarrow 0$  limit, the TDHF equation reduces to the Vlasov equation [15, 18]. In order to see this, it is useful to work with the Wigner transforms of  $\hat{\rho}$  and  $\hat{h}$ , which are the distribution function  $f(\mathbf{r}, \mathbf{p}, t)$  and the classical mean-field hamiltonian  $h(\mathbf{r}, \mathbf{p}, t)$ . For example, in the case of a purely local mean field  $U$ , the latter can be written as

$$h(\mathbf{r}, \mathbf{p}, t) = \frac{p^2}{2m} + U(\mathbf{r}, t). \quad (2)$$

Note that the mean field  $U$  depends on time through the time dependence of the density. To leading order in  $\hbar$ , the Wigner transform of the commutator in Eq. (1) reduces to the Poisson bracket of the corresponding Wigner transforms, and one obtains the Vlasov equation

$$\dot{f} = \{h, f\} = \frac{\partial h}{\partial \mathbf{r}} \cdot \frac{\partial f}{\partial \mathbf{p}} - \frac{\partial h}{\partial \mathbf{p}} \cdot \frac{\partial f}{\partial \mathbf{r}}. \quad (3)$$

A discussion of the Vlasov equation as limiting case of more general transport equations can be found in Ref. [21].

### B. Numerical method

In order to solve the Vlasov equation (3) numerically, we will employ the test-particle method which has often been used for the description of heavy-ion collisions [18, 22]. The basic idea of this method is to replace the distribution function  $f(\mathbf{r}, \mathbf{p}, t)$  by a finite number of delta functions (“test particles”)

$$f(\mathbf{r}, \mathbf{p}, t) = \frac{1}{\mathcal{N}} \sum_{i=1}^{\mathcal{N}A} \delta(\mathbf{r} - \mathbf{r}_i(t)) \delta(\mathbf{p} - \mathbf{p}_i(t)), \quad (4)$$

where  $\mathcal{N}$  denotes the number of test particles per nucleon and  $A$  is the mass number of the nucleus. In order to satisfy the Pauli principle, the density of test particles of each species ( $\alpha = n, p$ ) in phase-space must not exceed  $2\mathcal{N}/(2\pi\hbar)^3$  (the factor of 2 is the spin degeneracy). Inserting Eq. (4) into Eq. (3), one finds that each test particle has to follow its classical trajectory given by

$$\dot{\mathbf{r}}_i = \frac{\partial h(\mathbf{r}_i, \mathbf{p}_i, t)}{\partial \mathbf{p}_i}, \quad \dot{\mathbf{p}}_i = -\frac{\partial h(\mathbf{r}_i, \mathbf{p}_i, t)}{\partial \mathbf{r}_i}. \quad (5)$$

In the case of a purely local mean field, the equations of motion reduce to

$$\dot{\mathbf{r}}_i = \frac{\mathbf{p}_i}{m}, \quad \dot{\mathbf{p}}_i = -\nabla U(\mathbf{r}_i, t). \quad (6)$$

It is clear that these equations of motion prevent the test particles from entering the classically forbidden region. Note that this absence of tunneling is inherent to the Vlasov equation and independent of the numerical method.

The density  $\rho(\mathbf{r}, t)$  corresponding to the distribution function (4) is a sum of delta functions and hence not suitable for any practical calculation. In order to obtain a well-defined density which can be used, e.g., for the calculation of the mean field  $U$ , it is common to replace the delta functions in Eq. (4) by Gaussians [22, 23], leading to a smooth density

$$\tilde{\rho}(\mathbf{r}, t) = \sum_{i=1}^{\mathcal{N}A} \frac{e^{-(\mathbf{r}-\mathbf{r}_i(t))^2/d^2}}{\mathcal{N}(\sqrt{\pi}d)^3}. \quad (7)$$

For the sake of consistency, if one uses the smooth density  $\tilde{\rho}(\mathbf{r})$  in the calculation of the mean field  $U(\mathbf{r})$ , one

<sup>1</sup> Protons and neutrons have of course different density matrices  $\hat{\rho}_p$  and  $\hat{\rho}_n$ , different mean-field hamiltonians  $\hat{h}_p$  and  $\hat{h}_n$ , etc. In order to improve the readability, isospin indices  $\alpha = p, n$  are omitted in this paper except when they cannot be avoided.

has to modify also the acceleration equation and replace the force at  $\mathbf{r}_i$  by a force averaged over the Gaussian [22, 23],

$$\dot{\mathbf{p}}_i = -\nabla \tilde{U}(\mathbf{r}_i, t), \quad (8)$$

where

$$\tilde{U}(\mathbf{r}, t) = \int \frac{d^3s}{(\sqrt{\pi}d)^3} e^{-s^2/d^2} U(\mathbf{r} - \mathbf{s}, t). \quad (9)$$

Contrary to quantum molecular dynamics (QMD) [24] and related approaches, where similar Gaussians (in  $\mathbf{r}$  and  $\mathbf{p}$  space) are used to simulate quantum effects, we wish to stay here in the semiclassical framework and therefore do not attach any profound meaning to the smoothed density  $\tilde{\rho}$ . We consider it as an auxiliary quantity one has to introduce in the test-particle approach in order to be able to calculate well-defined densities and mean fields. As we will see in the next subsection, an interesting aspect of the smoothing of densities and mean fields is that it acts exactly like a finite-range interaction.

### C. Interaction

Until now, the mean field  $U$  entering the hamiltonian  $h$  has not been specified. On the one hand, it should be local for simplicity, and on the other hand, it should not be too simplistic if one wants to describe exotic nuclei. In this work, it will be derived from the bulk part  $E_{\text{int}}^\infty[\rho_p, \rho_n]$  of the Barcelona-Catania-Paris (BCP) energy functional [20], which is a parametrization of Brückner G-matrix results for nuclear and neutron matter. If the interaction energy is written as

$$E_{\text{int}}^\infty[\rho_p, \rho_n] = \int d^3r \epsilon_{\text{int}}^\infty(\rho_p, \rho_n), \quad (10)$$

the mean fields for protons ( $\alpha = p$ ) and neutrons ( $\alpha = n$ ) are given by

$$U_\alpha(\rho_p, \rho_n) = \frac{\partial \epsilon_{\text{int}}^\infty}{\partial \rho_\alpha}. \quad (11)$$

As explained in Sec. IIB,  $U$  is calculated from the smoothed densities  $\tilde{\rho}$ , i.e.,

$$U_\alpha(\mathbf{r}, t) = U_\alpha(\tilde{\rho}_p(\mathbf{r}, t), \tilde{\rho}_n(\mathbf{r}, t)). \quad (12)$$

In addition to the bulk part  $E_{\text{int}}^\infty$ , the BCP functional contains a finite-range part  $E_{\text{int}}^{\text{FR}}$ , a spin-orbit part  $E^{\text{s.o.}}$ , and a Coulomb part  $E_C$ . The finite-range part, which was introduced in Ref. [20] in order to get the right surface energy, has mainly the effect to smooth out the mean fields as compared to the densities. The same effect can be achieved without any additional term  $E_{\text{int}}^{\text{FR}}$  if one introduces a finite range into the bulk term  $E_{\text{int}}^\infty$ . For instance, in the latest version of the BCP functional [26],  $E_{\text{int}}^{\text{FR}}$  has been substituted by a finite range in the quadratic term of  $E_{\text{int}}^\infty$ .

Here, instead of implementing directly a finite-range force between the test particles, we first calculate the smooth density by folding the distribution function with a Gaussian of width  $d$  [Eq. (7)]. From this smoothed density, we calculate the mean field [Eq. (12)] which is folded again by a Gaussian of width  $d$  when the force on a particle is calculated [Eq. (9)]. If  $\epsilon_{\text{int}}^\infty$  was quadratic in the densities, this procedure would be equivalent to a Gaussian finite-range interaction with width  $\sqrt{2}d$ . Hence, if we choose  $d = 0.7$  fm, this corresponds roughly to the range  $r_0 = 1.05$  fm [20] of the finite-range term in the BCP functional.

For the sake of simplicity, the spin-orbit and Coulomb contributions,  $E^{\text{s.o.}}$  and  $E_C$ , will be neglected in the present work. Note that, according to the Kohn-Sham energy density functional theory, the BCP energy functional does not introduce an effective mass  $m^*$  in the kinetic energy part. Hence, the mass  $m$  which appears in the hamiltonian  $h$  is the free nucleon mass.

With the present prescription to calculate the force on a test particle, it is straight-forward to show that the total energy defined by

$$E_{\text{tot}} = \frac{1}{N} \sum_{i=1}^{NA} \frac{p_i^2}{2m} + E_{\text{int}}^\infty[\tilde{\rho}_p, \tilde{\rho}_n] \quad (13)$$

is exactly conserved during the time evolution.

### D. Ground state initialization

For a given initial distribution function  $f(\mathbf{r}, \mathbf{p}, t = t_0)$ , the time evolution at  $t > t_0$  is completely determined by Eq. (3). Here, we choose as initial state an isolated nucleus at rest in its ground state. An obvious requirement for the ground state is that it must be stationary. In the present framework, this means that the ground state must be calculated within the TF approximation,  $f(\mathbf{r}, \mathbf{p}) = \theta(\mu - h(\mathbf{r}, \mathbf{p}))$ , which is stationary under the Vlasov equation (3). Here,  $\theta$  is the step function and  $\mu$  is the chemical potential (Fermi energy). For consistency, since the numerical simulation of the Vlasov equation requires to smooth the densities and mean fields with Gaussians, Eqs. (7) and (9), the same Gaussians should be included in the calculation of the TF ground state [23].

Written explicitly, the equations which have to be solved self-consistently are

$$\rho(\mathbf{r}) = \frac{[2m(\mu - \tilde{U}(\mathbf{r}))]^{3/2}}{3\pi^2\hbar^3} \theta(\mu - \tilde{U}(\mathbf{r})), \quad (14)$$

$$\tilde{\rho}(\mathbf{r}) = \int \frac{d^3s}{(\sqrt{\pi}d)^3} e^{-s^2/d^2} \rho(\mathbf{r} - \mathbf{s}), \quad (15)$$

where  $\tilde{U}$  is computed from  $\tilde{\rho}$  according to Eqs. (12) and (9). The chemical potentials (Fermi energies)  $\mu_p$  and  $\mu_n$  are determined from the conditions

$$Z = \int d^3r \rho_p(\mathbf{r}), \quad N = \int d^3r \rho_n(\mathbf{r}). \quad (16)$$

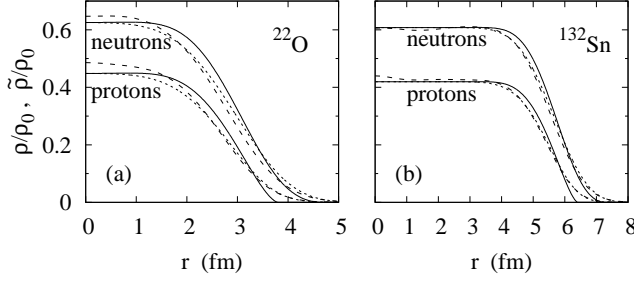


FIG. 1: Ground-state densities of neutrons and protons in units of  $\rho_0 = 0.17 \text{ fm}^{-3}$  in  $^{22}\text{O}$  (a) and  $^{132}\text{Sn}$  (b). Solid lines: self-consistent TF densities  $\rho(r)$ , dots: corresponding smoothed densities  $\tilde{\rho}(r)$  according to Eq. (15), dashes: smoothed densities  $\tilde{\rho}(r)$  after a simulation time of  $t = 2000 \text{ fm}/c$ .

For illustration, the density distributions of protons and neutrons in  $^{22}\text{O}$  and  $^{132}\text{Sn}$  obtained in this way are displayed in Fig. 1. The neutron skin is clearly visible in both cases. Note that the TF densities (solid lines) vanish at the classical turning points which are determined by  $\mu_\alpha = \tilde{U}_\alpha$ . The finite surface thickness stems from the self-consistent solution of the TF equations as described by Eqs. (14), (15), (12), and (9) with  $d = 0.7 \text{ fm}$ .

Once the self-consistent TF density distributions are obtained, the test particle positions  $\mathbf{r}_i$  are initialized randomly according to a probability density  $P(\mathbf{r}_i) \propto \rho(\mathbf{r}_i)$ . Then, the momenta  $\mathbf{p}_i$  are initialized randomly in a sphere with radius  $p_F(\mathbf{r}_i) = \hbar(3\pi^2\rho(\mathbf{r}_i))^{1/3}$  in order to correctly describe the Fermi motion. Remember that, if the Pauli principle is satisfied initially, it is preserved by the Vlasov dynamics due to Liouville's theorem [22].

### E. Numerical parameters and stability

As mentioned before, the width  $d$  of the Gaussians has two effects: first, it is necessary to obtain a well-defined density distribution, and second, it induces effectively a finite-range in the interaction. Most of the results to be presented in this paper were obtained with  $d = 0.7 \text{ fm}$ , leading to a reasonable smoothing of the mean field as discussed in Secs. II C and II D. This defines the minimum number of test particles to be used, as there must be a sufficiently large number of test particles per volume  $d^3$ , otherwise the statistical fluctuations become too strong. Here,  $\mathcal{N} = 2000$  test particles per particle were used. The equations of motion were solved with the velocity Verlet algorithm [25] using a time step of  $0.1 \text{ fm}/c$ . After each time step, the mean field  $U$  was updated and stored in a three dimensional grid with spacing  $0.4 \text{ fm}$ .

With these parameters, it was possible to ensure the stability of nuclei with large neutron excess, i.e., with very weakly bound neutrons in the surface, during the long simulation time of  $2000 \text{ fm}/c$  which is necessary for the calculation of the response function (see next subsection). The numerical losses due to test particles which

escape from the nucleus are  $< 1.3$  neutrons in the case of  $^{22}\text{O}$  and  $< 4$  neutrons in the case of  $^{132}\text{Sn}$ . In order to illustrate the stationarity of the ground state, we display in Fig. 1 the angle-averaged (see appendix) smoothed densities  $\tilde{\rho}$  corresponding to the test-particle distribution after the simulation (dashes), which agree very well with those calculated during the initialization (dots). During the simulation, the kinetic energy (including that carried away by the test particles escaping from the nucleus) drops by  $\sim 5\%$  in the case of  $^{22}\text{O}$  and by  $\sim 2\%$  in the case of  $^{132}\text{Sn}$ . The relative variation of the total (kinetic plus interaction) energy is of the order of  $10^{-6}$ .

In order to check that the results do not depend sensitively on the value of the width parameter  $d$ , some calculations with  $d = 0.5 \text{ fm}$  were performed. In this case, the number of test particles per particle was increased to  $\mathcal{N} = 5000$  in order to limit statistical fluctuations, and the spacing of the grid for the mean field was reduced to  $0.3 \text{ fm}$ .

### F. Calculation of the response function

Within the present approach, the collective modes are described as time-dependent oscillations of the nucleus after a perturbation of the ground state. In order to relate these oscillations to the usual response function, which is defined in terms of transition probabilities from the ground state to excited states, let us temporarily leave the semiclassical framework and return to quantum mechanics. We consider a perturbation hamiltonian of the form  $\hat{H}_{\text{ex}}(t) = \lambda \hat{Q} \delta(t)$ , where  $\hat{Q}$  is the excitation operator we want to study and  $\lambda$  is supposed to be small. Then, within linear response theory [27], the expectation value of the operator  $\hat{Q}$  as a function of time is given by

$$\begin{aligned} \delta\langle\hat{Q}\rangle(t) &= \langle\hat{Q}\rangle(t) - \langle 0|\hat{Q}|0\rangle \\ &= -\frac{2\lambda\theta(t)}{\hbar} \sum_f |\langle f|\hat{Q}|0\rangle|^2 \sin\frac{(E_f - E_0)t}{\hbar}, \end{aligned} \quad (17)$$

where  $|0\rangle$  is the ground state (of the unperturbed hamiltonian  $\hat{H}$ ),  $|f\rangle$  is an excited state, and  $E_0$  and  $E_f$  are the corresponding energies. Defining the strength function as usual by

$$S(E) = \sum_f |\langle f|\hat{Q}|0\rangle|^2 \delta(E - E_f + E_0), \quad (18)$$

we can obtain it from  $\delta\langle\hat{Q}\rangle(t)$  via a Fourier transform

$$S(E) = -\frac{1}{\pi\lambda} \int_0^\infty dt \delta\langle\hat{Q}\rangle(t) \sin\frac{Et}{\hbar}. \quad (19)$$

Let us now return to the semiclassical framework. Under the assumption that  $\hat{Q}$  is a one-body operator, i.e.

$$\hat{Q} = \sum_{i=1}^A \hat{q}_i. \quad (20)$$



one can calculate its expectation value as

$$\langle \hat{Q} \rangle(t) = \int d^3r d^3p f(\mathbf{r}, \mathbf{p}, t) q(\mathbf{r}, \mathbf{p}), \quad (21)$$

where  $q(\mathbf{r}, \mathbf{p})$  is the Wigner transform of  $\hat{q}$ , which can be obtained (at least to leading order in the  $\hbar$  expansion [15]) by replacing the operators  $\hat{\mathbf{r}}$  and  $\hat{\mathbf{p}}$  in  $\hat{q}$  by their classical counterparts  $\mathbf{r}$  and  $\mathbf{p}$ . In terms of the test particle positions and momenta, this expectation value can be expressed as

$$\langle \hat{Q} \rangle(t) = \frac{1}{N} \sum_{i=1}^{NA} q(\mathbf{r}_i(t), \mathbf{p}_i(t)). \quad (22)$$

The last point which remains to be explained is how the delta function perturbation at  $t = 0$  changes the initial distribution function, i.e., in our simulation, the distribution of test particles. In principle, one has to solve the classical equations of motion (5) with the perturbed hamiltonian  $h + \lambda q \delta(t)$  instead of  $h$ . Replacing the delta function by a short pulse of length  $\delta t$ , one can show that in the limit  $\delta t \rightarrow 0$  and to leading order in  $\lambda$ , the effect of the perturbation is to change the positions and momenta of the test particles as follows<sup>2</sup>:

$$\mathbf{r}_i \rightarrow \mathbf{r}_i + \lambda \frac{\partial q(\mathbf{r}_i, \mathbf{p}_i)}{\partial \mathbf{p}_i}, \quad \mathbf{p}_i \rightarrow \mathbf{p}_i - \lambda \frac{\partial q(\mathbf{r}_i, \mathbf{p}_i)}{\partial \mathbf{r}_i}. \quad (23)$$

To summarize the procedure: First, the test-particle distribution at  $t = 0$  is initialized as explained in Sec. IID. Then the test-particle positions and momenta are changed according to Eq. (23) and the mean field  $U$  is recalculated if necessary (if the excitation operator  $q$  depends on  $\mathbf{p}$ ). After that, the equations of motion (6) are solved simultaneously for all test particles, and the mean field  $U$  is updated after each time step. In this way, one obtains the expectation value  $\langle \hat{Q} \rangle(t)$  as a function of time, and its Fourier transform (19) gives the strength function  $S(E)$ .

In practice, it is of course impossible to run the simulation to  $t = \infty$ . Here, the simulations will be stopped at  $t_{\max} = 2000$  fm/c. In order to avoid oscillations in the Fourier transform related to the cut at  $t_{\max}$ , the strength function  $S(E)$  will be folded with a Lorentzian of width  $\gamma = 0.5$  MeV, which is equivalent to multiplying the sine function in Eq. (19) by  $e^{-\gamma t/2\hbar}$ .

### G. Transition densities and velocity fields

The delta function perturbation at  $t = 0$  excites simultaneously all modes which can be excited by the operator  $\hat{Q}$ . It is therefore difficult to extract the transition density

and velocity field corresponding to one particular mode. What can be done is to calculate the (smoothed) density distributions  $\tilde{\rho}(\mathbf{r}, t)$  and velocities

$$\mathbf{v}(\mathbf{r}, t) = \frac{\tilde{\mathbf{j}}(\mathbf{r}, t)}{\tilde{\rho}(\mathbf{r}, t)} = \frac{1}{\tilde{\rho}(\mathbf{r}, t)} \sum_{i=1}^{NA} \frac{\mathbf{p}_i(t)}{m} \frac{e^{(\mathbf{r}-\mathbf{r}_i(t))^2/d^2}}{\mathcal{N}(\sqrt{\pi}d)^3} \quad (24)$$

(see appendix for more details) as functions of time.

In the case of a time-even excitation operator, i.e.,  $q(\mathbf{r}, \mathbf{p}) = q(\mathbf{r}, -\mathbf{p})$ , the particles get a kick in momentum space and the oscillation starts with maximum velocity, while the density is not changed at  $t = 0$ . The situation is opposite if the excitation operator is time-odd, i.e.,  $q(\mathbf{r}, \mathbf{p}) = -q(\mathbf{r}, -\mathbf{p})$ : In this case, the velocity is zero at  $t = 0$ , while the density is immediately changed due to the displacement of the particles in coordinate space.

In order to find the contribution of a given mode to the density and velocity oscillations, one has to choose the energy  $E$  corresponding to a peak in the strength function and compute the transition densities and velocity fields as a Fourier transform of  $\tilde{\rho}(\mathbf{r}, t)$  and  $\mathbf{v}(\mathbf{r}, t)$ , respectively. In the case of a time-even excitation operator, one has to use

$$\delta \tilde{\rho}(\mathbf{r}, E) \propto \int_0^\infty dt \tilde{\rho}(\mathbf{r}, t) \sin \frac{Et}{\hbar}, \quad (25)$$

$$\mathbf{v}(\mathbf{r}, E) \propto \int_0^\infty dt \mathbf{v}(\mathbf{r}, t) \cos \frac{Et}{\hbar}, \quad (26)$$

whereas in the case of a time-odd operator, the sine and cosine functions must be interchanged. In practice, since the simulation runs only to  $t_{\max} = 2000$  fm/c, the sine and cosine functions are multiplied by an exponential damping factor  $e^{-\gamma t/2\hbar}$ ,  $\gamma = 0.5$  MeV, as in the strength function  $S(E)$ .

It should be noted that even if the energy  $E$  corresponds to a peak in  $S(E)$ , the transition densities and velocity fields obtained with this method may still contain contributions from other modes if those have a width which makes their spectrum extend to energy  $E$ .

## III. RESULTS FOR THE PYGMY RESONANCE

### A. Electric dipole response

Since the pygmy resonance is often studied in  $(\gamma, \gamma')$  experiments, we consider as excitation operator the electric dipole operator [28]

$$q = \begin{cases} \frac{N}{A} z & \text{for protons,} \\ -\frac{Z}{A} z & \text{for neutrons,} \end{cases} \quad (27)$$

which is defined such that the center of mass of the nucleus stays at rest. For the parameter  $\lambda$  multiplying the operator  $q$ , the value  $\lambda = 25$  MeV/c is chosen as a compromise to excite an oscillation which is much larger than

<sup>2</sup> If  $q$  depends only on  $\mathbf{r}$  or only on  $\mathbf{p}$ , this result is valid to all orders in  $\lambda$ .

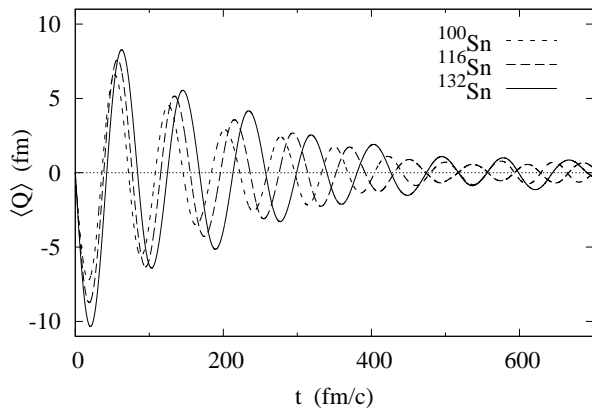


FIG. 2: Electric dipole moment of  $^{100}\text{Sn}$ ,  $^{116}\text{Sn}$ , and  $^{132}\text{Sn}$  after a perturbation with  $\hat{H}_{\text{ex}}(t) = \lambda \hat{Q} \delta(t)$ ,  $\hat{Q}$  being the electric dipole operator and  $\lambda = 25$  MeV/c.

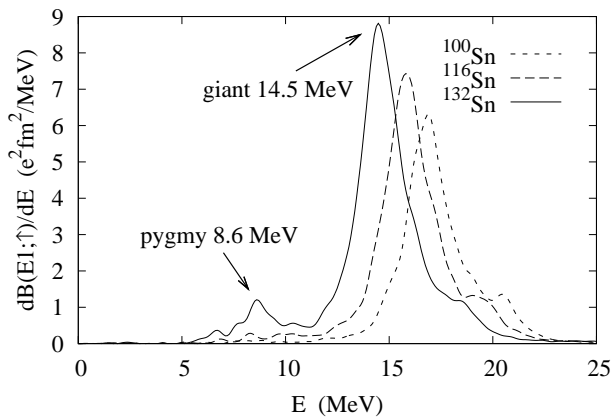


FIG. 3: Electric dipole strength of  $^{100}\text{Sn}$ ,  $^{116}\text{Sn}$ , and  $^{132}\text{Sn}$ .

the numerical noise due to the finite number of test particles, but still small enough so that nonlinearities do not play a role. Calculations for different nuclei from oxygen isotopes up to  $^{208}\text{Pb}$  were performed. The existence of the PDR as a small enhancement in the strength function well below the energy of the GDR turned out to be a general property of  $N > Z$  nuclei, while it is absent in  $N = Z$  nuclei.

As a first example, let us discuss the results obtained for the three tin isotopes  $^{100}\text{Sn}$ ,  $^{116}\text{Sn}$ , and  $^{132}\text{Sn}$ . In all three cases, after initializing and exciting the nucleus, one observes a damped oscillation of  $\langle \hat{Q} \rangle(t)$  with the frequency of the GDR, see Fig. 2. The curves look qualitatively similar for all three nuclei, and in order to see anything else than the GDR, one has to look at their Fourier transforms. In Fig. 3, the corresponding electric dipole strengths are displayed. In all three nuclei, there is a very strong peak at around 14.5 MeV ( $^{132}\text{Sn}$ ) to 16.7 MeV ( $^{100}\text{Sn}$ ) corresponding to the GDR. The energies of the GDR are in reasonable agreement with experimental values, whereas the widths are much too small. For instance, the curve shown for  $^{116}\text{Sn}$  is very well fitted by

a Lorentzian with energy 15.8 MeV and width 2.4 MeV (which includes the artificial width  $\gamma = 0.5$  MeV mentioned in the end of Sec. II F), whereas the corresponding experimental energy and width are 15.67 and 4.19 MeV, respectively [29].

It is in fact not surprising that the widths are too small. Since in the linear regime the Vlasov equation is a semiclassical version of the RPA [16, 17], the only damping mechanism that is present here is Landau damping. The fact that in an anharmonic potential different classical orbits have different periodicities leads to effects which are completely analogous to the splitting of the quantum mechanical single-particle levels, as already noticed in Refs. [16, 17]. The main difference to quantum mechanical RPA calculations is that within Vlasov dynamics the strength is not fragmented into many discrete states, but it is continuous<sup>3</sup>. The fragmentation due to the coupling to more complex states like two-phonon or two-particle-two-hole states is missing here, as it is in RPA [30]. In the semiclassical framework, effects analogous to two-particle-two-hole excitations can be included via a collision term [17], but this is beyond the scope of the present work.

Let us return to the discussion of the results shown in Fig. 3. In the case of  $^{116}\text{Sn}$ , one can see a small amount of dipole strength below the GDR which is absent in the  $N = Z$  nucleus  $^{100}\text{Sn}$  and which becomes a well defined peak at 8.6 MeV in the case of  $^{132}\text{Sn}$ . This peak corresponds to the PDR. For comparison, in experiment, it was seen in  $^{130}\text{Sn}$  and  $^{132}\text{Sn}$  at a slightly higher energy of approximately 9.8 MeV [31]. Subtracting the tail of the GDR (assuming that it has the same shape as in  $^{100}\text{Sn}$ ), one finds that in  $^{132}\text{Sn}$  the PDR contributes about 4% to the energy-weighted sum rule (EWSR), which happens to be in perfect agreement with the experimental value from Ref. [31]. However, the experimental number for  $^{130}\text{Sn}$  is larger (7% of the EWSR) than that for  $^{132}\text{Sn}$  although the neutron excess is smaller, certainly due to the doubly magic nature of  $^{132}\text{Sn}$ . In a theory without shell effects, the results for  $^{130}\text{Sn}$  and  $^{132}\text{Sn}$  are of course almost identical. Nevertheless this comparison shows that, in spite of its crudeness, the semiclassical approach is capable of giving the right order of magnitude for the transition strength.

In order to see how sensitive these results are to the choice of the width parameter  $d$ , the calculation for  $^{132}\text{Sn}$  was repeated with  $d = 0.5$  instead of 0.7 fm. The main effect of this change on the electric dipole response is that the GDR is slightly shifted from 14.5 to 15.3 MeV. The position of the PDR is almost not affected (the maximum of the peak is shifted from 8.6 to 8.7 MeV). The height of

<sup>3</sup> Note that in Refs. [16, 17] the angular momentum of the classical orbits was artificially quantized in order to simplify the practical calculations and to obtain a discrete spectrum as in RPA. In the present work, the angular momentum of the test particles is arbitrary, which results in a continuous spectrum.

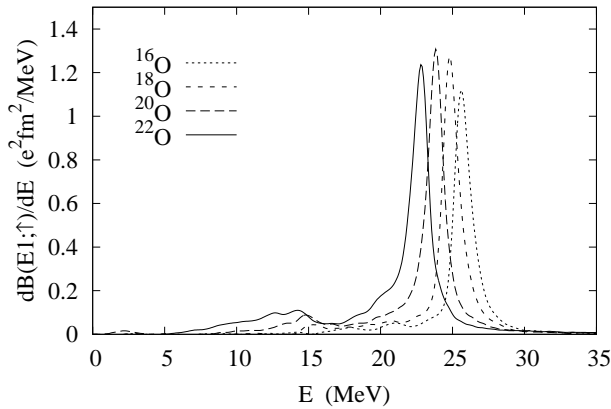


FIG. 4: Electric dipole strength of  $^{16}\text{O}$ ,  $^{18}\text{O}$ ,  $^{20}\text{O}$ , and  $^{22}\text{O}$ .

the peak corresponding to the PDR is slightly reduced, but subtracting the tail of the GDR, which is now further apart, one finds again that it contributes about 4% of the EWSR. The shape of the transition densities and velocity fields (see next subsection) of the two modes are not changed either, except that they go to zero more rapidly at the surface. The conclusion is that the results do not depend strongly on the parameter  $d$ , and from now on we will keep  $d = 0.7$  fm which is the value motivated in Sec. II C.

As a second example let us consider the even oxygen isotopes from  $^{16}\text{O}$  to  $^{22}\text{O}$ . The corresponding strength functions are displayed in Fig. 4. As in the case of tin isotopes, it can be seen that with increasing neutron excess some strength builds up at low energies, which is clearly separated from the GDR. Quantitatively, if integrated up to 15 MeV, its contribution to the EWSR is 0% for  $^{18}\text{O}$ , 4% for  $^{20}\text{O}$ , and 8% for  $^{22}\text{O}$ . This has to be compared with the corresponding experimental numbers which are 8% for  $^{18}\text{O}$ , 12% for  $^{20}\text{O}$ , and 7% for  $^{22}\text{O}$  [32]. It is interesting to notice that, as in the case of  $^{130}\text{Sn}$  and  $^{132}\text{Sn}$ , the experimental results for the contribution of the low-lying strength to the EWSR do not increase with increasing neutron excess. This must be related to shell effects and cannot be reproduced within the semiclassical framework. Unlike in  $^{132}\text{Sn}$ , the low-lying strength distribution in  $^{22}\text{O}$  is completely spread and does not have a clear peak. In this case, it does not seem to be appropriate to speak of the pygmy resonance as a collective mode.

Finally, let us discuss some numbers for the nucleus  $^{208}\text{Pb}$ . The response (not shown) looks qualitatively similar to the  $^{132}\text{Sn}$  case: the pygmy resonance shows up as a well-defined peak. This peak is situated at 7.6 MeV, while the experimental spectrum has two groups of transitions around 5.3 and 7.3 MeV [8]. The result for the total strength  $B(E1; \uparrow)$  integrated up to 8 MeV is  $2 e^2 \text{fm}^2$  within Vlasov and  $1.32 e^2 \text{fm}^2$  in the experiment [8].

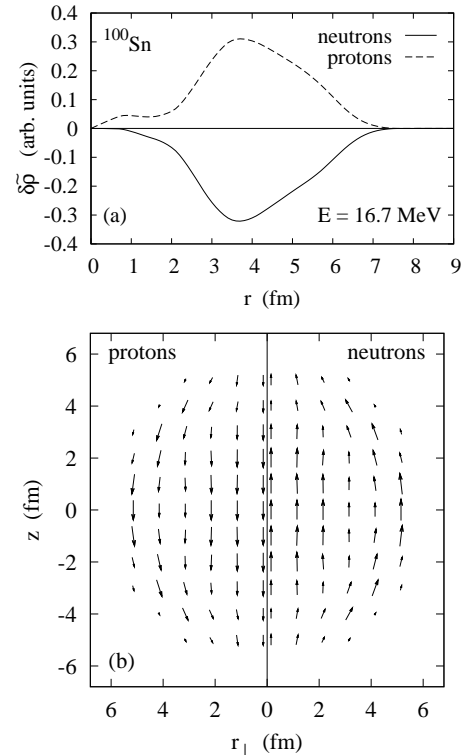


FIG. 5: (a) Transition densities  $\delta\tilde{\rho}_p$  (dashes) and  $\delta\tilde{\rho}_n$  (solid line) and (b) velocity fields  $\mathbf{v}_p$  (left) and  $\mathbf{v}_n$  (right) corresponding to the GDR in  $^{100}\text{Sn}$ .

## B. Velocity fields and transition densities

In order to study the nature of the collective modes, it is useful to look at the transition densities and the velocity fields. The graphical representation of the transition density can be simplified by assuming that the amplitude of the oscillation is weak (linear response regime). In this case, the spherical symmetry of the ground state and the dipole form of the excitation operator imply that the transition density can be written as  $\delta\tilde{\rho}(\mathbf{r}) = \delta\tilde{\rho}(r) \cos\theta$ , where  $r = |\mathbf{r}|$  and  $\cos\theta = z/r$ .

In order to test the calculation of transition densities and velocity fields, let us start with a simple example, namely with the GDR in the symmetric nucleus  $^{100}\text{Sn}$ . The results are shown in Fig. 5. As expected, protons and neutrons move against each other in  $z$  direction. The velocity (Fig. 5b) is not constant but decreases with increasing  $r$  and gets curved, almost as in the Steinwedel-Jensen model in which the radial component of the velocity field vanishes at the surface [14]. Since the Coulomb interaction is not included in the present calculation, the transition densities and velocity fields of neutrons and protons should be exactly opposite to each other. For the velocity fields (Fig. 5b), this seems to be the case, but in the transition densities (Fig. 5a) a discrepancy is present at small radii ( $\lesssim 2$  fm). This is clearly a numerical error. The reason is that at small radii, the angle

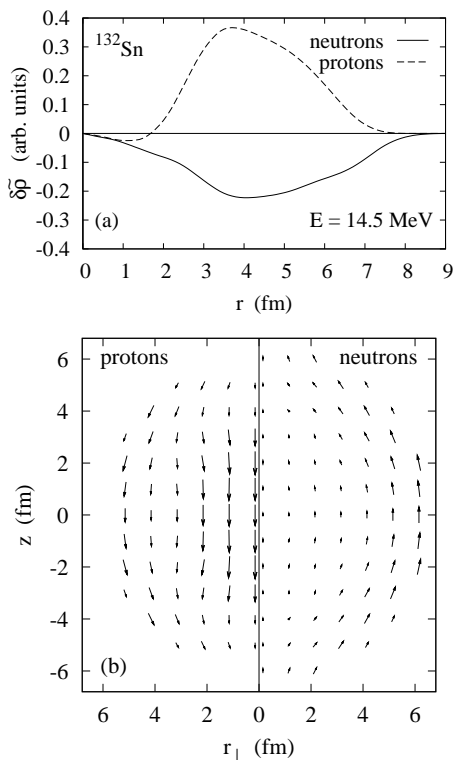


FIG. 6: Same as Fig. 5, but for the GDR in  $^{132}\text{Sn}$ .

averaging, which is implicit in the computation of the radial functions  $\delta\tilde{\rho}(r)$ , is less effective in reducing statistical fluctuations than at large radii. Since the amplitude of the oscillation is very small, already small statistical fluctuations of the density can lead to an erroneous result for the transition density. This is why the transition densities at  $r \lesssim 2$  fm cannot be trusted.

After this word of caution, let us look at the more interesting case of the neutron rich nucleus  $^{132}\text{Sn}$ . Since in this nucleus the neutron and proton density distributions in the ground state are different, one does not expect any more that the transition densities and velocity fields of neutrons and protons are exactly opposite to each other. Generally speaking, in  $N \neq Z$  nuclei, even in the absence of Coulomb interaction, the collective modes are not exactly isovector or isoscalar ones, but they have both isovector and isoscalar components. Let us first discuss the GDR which is displayed in Fig. 6. Since the transition densities for  $r \lesssim 2$  fm are not reliable, the node of  $\delta\tilde{\rho}_p$  (dashed line in Fig. 6a) is most likely a numerical error. Beyond that radius, the shape of the transition densities is typical for the GDR. As a consequence of the neutron skin, the transition density of neutrons extends to larger radii than that of protons. The velocity fields (Fig. 6b) are more surprising: While the proton velocity is very similar to the one in  $^{100}\text{Sn}$ , the neutron velocity is very different. It seems that in  $^{132}\text{Sn}$  the neutron velocity is strongly suppressed in the center and enhanced in the neutron skin. The origin of this phenomenon is

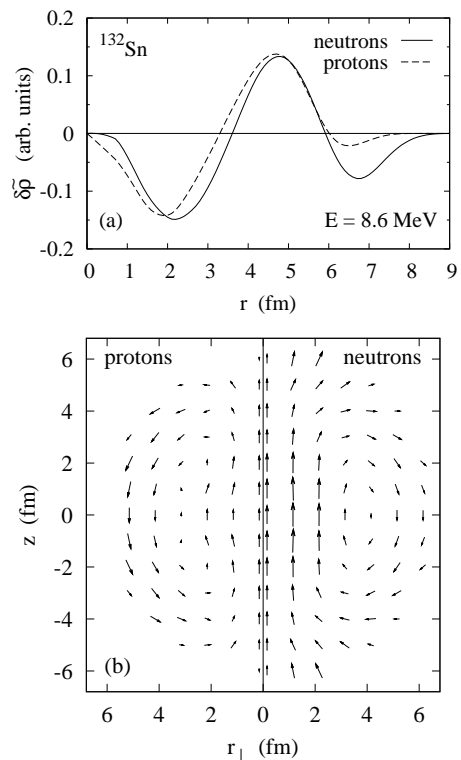


FIG. 7: Same as Fig. 5, but for the PDR in  $^{132}\text{Sn}$ .

not completely understood, but a possible explanation could be the coupling between the isovector GDR and the isoscalar torus mode, see next section.

In Fig. 7, the transition densities and velocity fields corresponding to the pygmy mode are displayed. As one can see, protons and neutrons oscillate mainly in phase. The isovector component of the pygmy mode comes from the different transition densities in the region of the neutron skin. The velocity field has a toroidal shape, very different from the giant resonance. Such a shape was already found in quantum mechanical calculations of the velocity field of the pygmy mode in  $^{122}\text{Zr}$  [6] and in  $^{208}\text{Pb}$  [8]. In the literature, it is often said that the PDR is an oscillation of the neutron skin against the  $N = Z$  core of the nucleus [1]. Due to the toroidal form of the velocity field, the neutrons in the neutron skin indeed move against the neutrons in the core. However, the image of the skin oscillating as a whole against an inert core seems to be over-simplified, since the protons have a toroidal flow-pattern, too.

## IV. RESULTS FOR THE TORUS MODE

### A. Toroidal excitation spectrum

Motivated by the toroidal shape of the velocity field of the PDR, let us have a closer look at the isoscalar torus



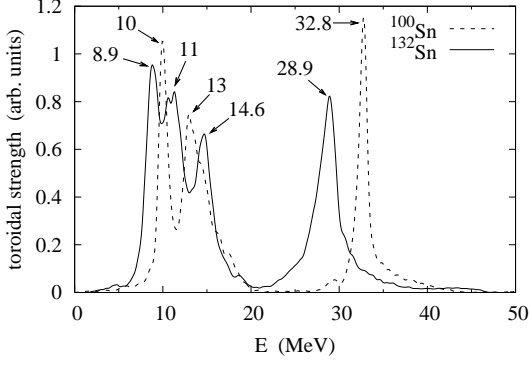


FIG. 8: Strength of the response of  $^{100}\text{Sn}$  and  $^{132}\text{Sn}$  to the toroidal dipole operator, Eq. (28).

mode. Its excitation operator is given by

$$q(\mathbf{r}, \mathbf{p}) = (2r^2 - \frac{5}{3}\langle r^2 \rangle) p_z - (\mathbf{p} \cdot \mathbf{r}) z. \quad (28)$$

Here, the term  $\propto \langle r^2 \rangle p_z$  has been added to the operator given in Ref. [11] in order to make sure that the excitation does not displace the center of mass of the nucleus. Note that, according to Eq. (23), this excitation operator leads to a change of both positions and momenta of the test particles at  $t = 0$  since it depends on  $\mathbf{r}$  and  $\mathbf{p}$ .

The corresponding strength functions of  $^{100}\text{Sn}$  and  $^{132}\text{Sn}$  are shown in Fig. 8. We see that the strength is split into two regions below and above  $\sim 20$  MeV. The first region contains two peaks at 10 and 13 MeV in the case of  $^{100}\text{Sn}$  and three peaks at 8.9, 11, and 14.6 MeV in the case of  $^{132}\text{Sn}$ . In the second region, there is an isolated peak at 32.8 MeV in the case of  $^{100}\text{Sn}$  and 28.9 MeV in the case of  $^{132}\text{Sn}$ . The nature of the different modes will be clarified by the analysis of the corresponding transition densities and velocity fields. It is interesting to notice that the positions of the modes in  $^{100}\text{Sn}$  at 10 and 32.8 MeV are in good agreement with recent RPA results obtained with the UCOM interaction [33]. The mode at 13 MeV corresponds probably to the fragmented strength concentrated around 15 MeV in the RPA response, see Fig. 1 of Ref. [33].

### B. Velocity fields and transition densities

In Figs. 9-12 the transition densities and velocity fields corresponding to the peaks of the toroidal dipole response of  $^{132}\text{Sn}$  at 8.9, 11, 14.6, and 28.9 MeV are shown. Let us first compare the results for the modes at 8.9 (Fig. 9) and 11 MeV (Fig. 10). At first glance, the velocity fields look similar for these two modes, but the transition densities are completely different. Both modes are essentially isoscalar. Comparing the results for the 8.9 MeV mode in Fig. 9 with the results for the PDR at 8.6 MeV in Fig. 7, we see a striking similarity. One can say that these two modes are in fact one and the same, only excited in two different ways. Note that the lines with

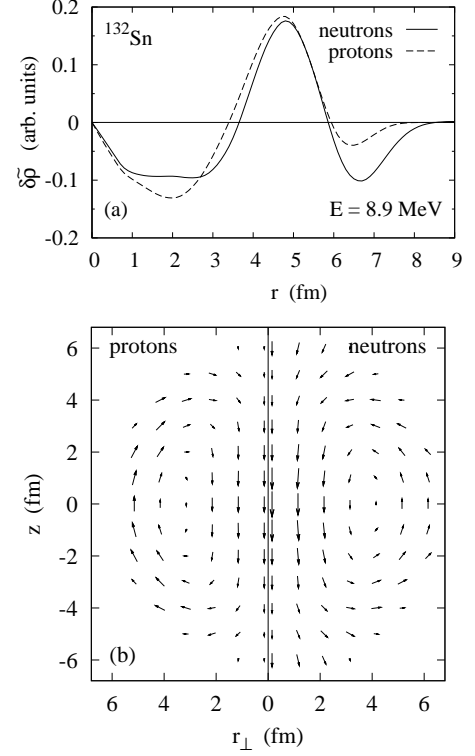


FIG. 9: Same as Fig. 5, but for the mode excited by the toroidal dipole operator at 8.9 MeV in  $^{132}\text{Sn}$ .

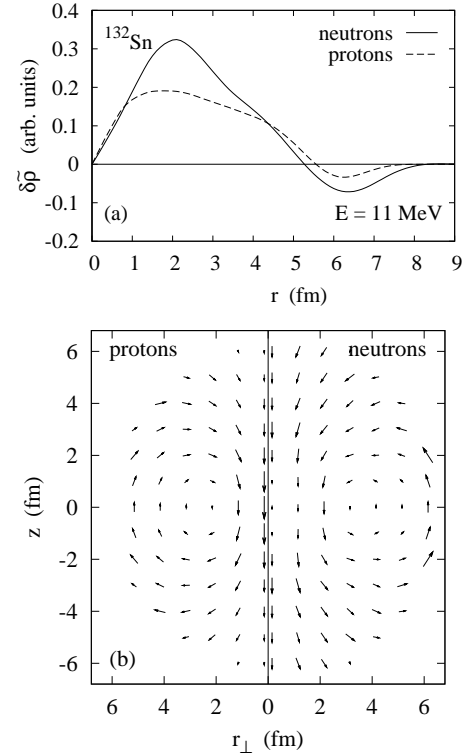


FIG. 10: Same as Fig. 5, but for the mode excited by the toroidal dipole operator at 11 MeV in  $^{132}\text{Sn}$ .

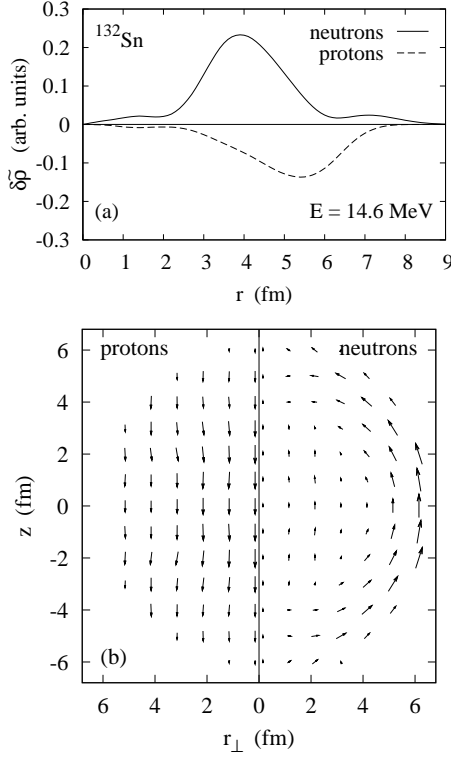


FIG. 11: Same as Fig. 5, but for the mode excited by the toroidal dipole operator at 14.6 MeV in  $^{132}\text{Sn}$ .

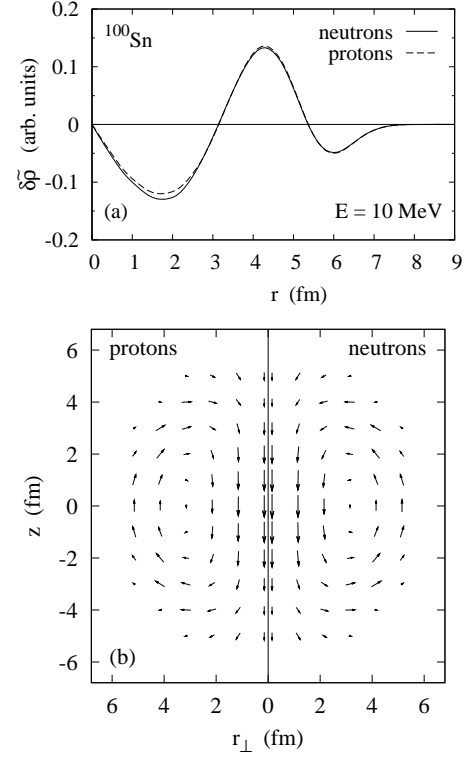


FIG. 13: Same as Fig. 5, but for the toroidal mode at 10 MeV in  $^{100}\text{Sn}$ .

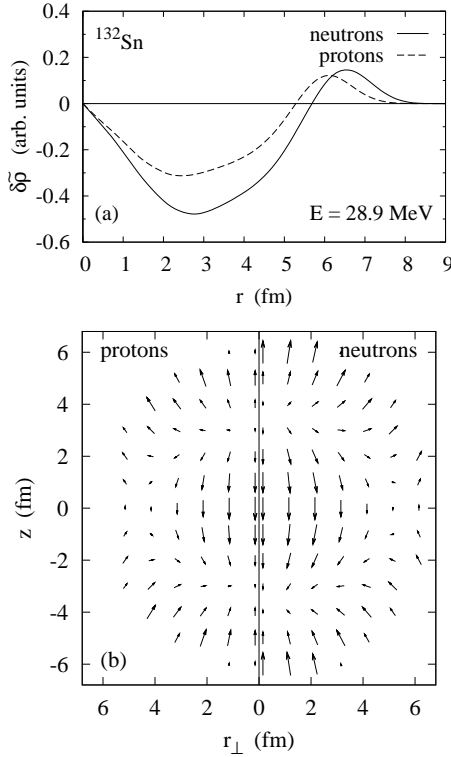


FIG. 12: Same as Fig. 5, but for the compressional dipole mode at 28.9 MeV in  $^{132}\text{Sn}$ .

zero velocity, around which the protons and neutrons circulate, are at  $\sim 3$  fm and  $\sim 4$  fm from the center of the nucleus, respectively, i.e., they lie inside the core of the nucleus and not in the surface. The velocity field of the mode at 11 MeV looks even more like a torus, since the shape of the velocity field is more rounded than in the mode at 8.9 MeV. What about the third mode at 14.6 MeV (Fig. 11)? First of all, from the transition densities, one sees that this mode has mainly isovector character. Comparing with the results for the GDR at 14.5 MeV in Fig. 6, one concludes that the mode at 14.6 MeV is in fact the GDR, which is excited by the isoscalar toroidal dipole operator due to the strong neutron excess in  $^{132}\text{Sn}$ . Finally, the high-lying isoscalar dipole mode at 28.9 MeV (Fig. 12) has a completely different nature. As can be seen from the velocity field, this mainly isoscalar mode exhibits a compressional motion, and for this reason it is usually called the compressional dipole mode.

In order to get a better understanding of the two low-lying modes at 8.9 and 11 MeV, let us look at the corresponding modes of  $^{100}\text{Sn}$  which lie at 10 and 13 MeV, see Figs. 13 and 14. We observe that the mode at 10 MeV in  $^{100}\text{Sn}$  (Fig. 13) has qualitatively the same velocity field and transition density as the mode corresponding to the PDR in  $^{132}\text{Sn}$  (Fig. 9). From this one may conclude that the existence of this mode does not require the presence of a neutron skin. The neutron excess is only needed in order to be able to probe this mode with the electric

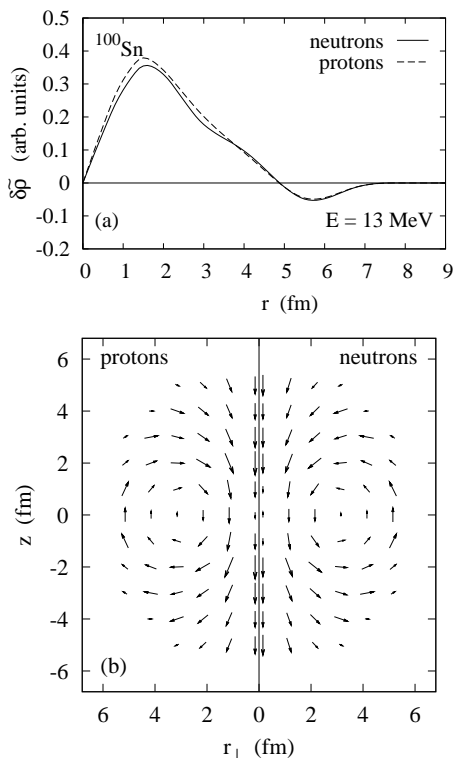


FIG. 14: Same as Fig. 5, but for the toroidal mode at 13 MeV in  $^{100}\text{Sn}$ .

dipole operator. Looking closely at the velocity field of this mode (Figs. 9 and 13), one realizes that the velocity field is almost constant in the center of the nucleus, contrary to the velocity field of the toroidal mode which lies at slightly higher energy [11 MeV in  $^{132}\text{Sn}$  (Fig. 10) and 13 MeV in  $^{100}\text{Sn}$  (Fig. 14), respectively]. This can be interpreted in the sense that the lower one of the two modes is an oscillation of the surface (not necessarily the neutron skin, since  $^{100}\text{Sn}$  does not have one) against the core, whereas the higher one is the original torus mode which, in the framework of nuclear fluid dynamics, exists already in a uniform sphere. This interpretation is corroborated by the transition densities, which in the case of the higher mode (Figs. 10 and 14) are much more concentrated in the inner part of the nucleus, while those of the lower mode (Figs. 9 and 13) are much stronger in the surface region. Another support for this interpretation is the energy of this mode: According to Ref. [12], in a uniform sphere and within nuclear fluid dynamics, the torus mode should lie at  $65 - 85A^{-1/3}$  MeV, i.e., at 14 – 18.3 MeV in the case of  $^{100}\text{Sn}$  and 12.8 – 16.7 MeV in the case of  $^{132}\text{Sn}$ . This is slightly higher, but not very far from the modes found here at 13 and 11 MeV, respectively.

## V. SUMMARY AND DISCUSSION

In this paper, electric and isoscalar dipole excitations were studied within the semiclassical TF plus Vlasov approach. As interaction, the bulk part of the BCP functional was employed, which was smoothed out in space in order to mimic the effect of the neglected finite-range term. The TF equation for the ground state as well as the Vlasov equation for the dynamics were solved numerically without any further simplifying assumptions. Compared to fully quantum mechanical Hartree-Fock plus RPA calculations, the present method is missing the shell effects, what can be useful if one is interested in generic properties and average trends.

The electric dipole response of oxygen and tin isotopes was discussed (calculations for other nuclei like calcium and lead were performed but not shown). In all cases, low-lying strength corresponding to the PDR was found in the very neutron-rich isotopes, however in the neutron-rich oxygen isotopes the strength was spread over a large energy range, in accordance with the strong fragmentation of the strength in quantum mechanical calculations [6], so that one cannot speak of a collective mode in this case. This shows that the existence of the PDR is a generic property of neutron-rich nuclei and does not rely on a specific structure of single-particle levels. In heavier nuclei, the PDR is found to be a collective excitation. The obtained energies and transition probabilities are roughly in agreement with experimental data (at least as well as it can be expected in a theory without shell effects). The transition densities and velocity fields of the pygmy mode were analysed and it was found that the velocity field has a toroidal shape, in agreement with the findings of earlier quantum mechanical calculations [6, 8]. The vortex line lies inside the core of the nucleus, and the torus can therefore be seen in both neutron and proton velocity fields, which suggests that the popular picture of the neutron skin oscillating against a static  $N = Z$  core is oversimplified.

In order to compare the PDR and the torus mode in detail, the response to the isoscalar toroidal operator was studied. In the example of  $^{132}\text{Sn}$  it was found that, due to the mixing of isoscalar and isovector modes, the predominantly isoscalar PDR and the predominantly isovector GDR can be seen in both the E1 and the toroidal strength functions. In addition, the toroidal response exhibits two peaks which do not show up in the electric dipole response: a second toroidal mode which lies slightly above the PDR, and a compressional dipole mode. The two toroidal modes exist also in the  $N = Z$  nucleus  $^{100}\text{Sn}$ . Hence, the existence of these modes, including the lower one which in the case of  $^{132}\text{Sn}$  was identified with the PDR, does not rely on the presence of a neutron skin. If this interpretation is correct, the reason why the PDR is only seen in nuclei with large neutron excess is simply that otherwise the E1 strength of this mode is too small to be seen. However, it was recently pointed out that, if the isospin symmetry breaking effect of the Coulomb

interaction is taken into account, a small contribution of this mode can be seen even in the electric dipole response of  $N = Z$  nuclei [33]). Another conclusion which can be drawn from this result is that the PDR, like the torus mode, cannot be described in a hydrodynamical picture, but its existence relies on the “elasticity” of the nuclear medium due to Fermi-surface deformation. This fact was also stressed in Ref. [34].

The two toroidal modes are apparently qualitatively different, although their velocity fields look quite similar: The higher mode corresponds to the torus mode of an elastic sphere, which has been discussed in the literature for many years [10, 12], whereas the lower one corresponds more to an oscillation of the core against the surface (but not necessarily against the neutron skin), qualitatively similar to the modes discussed in Ref. [34].

Of course, the present approach has some shortcomings and is not meant to replace more sophisticated quantum-mechanical calculations. Since it is a semiclassical formalism, shell effects cannot be described. On the one hand, this results in clear pictures for the different modes, but on the other hand, it is of course a simplification which makes the detailed comparison with experiment and with more realistic calculations difficult. In addition, a couple of approximations were made which give probably rise to systematic deviations. For example, the Coulomb interaction was omitted. One would also expect an important effect from pairing, since it affects in particular rotational motion and excitations involving Fermi surface deformation. Nevertheless, the obtained results are surprisingly reasonable and will maybe serve as a motivation for a more detailed study of the relationship between the pygmy and the torus mode within fully quantum mechanical approaches.

### Acknowledgments

I thank E. Balbutsev and P. Papakonstantinou for discussions and P. Schuck for numerous ideas, suggestions and careful reading of the manuscript. This work was supported by ANR (project NEXEN).

### Appendix A: Angle averaged densities and velocity fields

All simulations were done in three dimensions without any imposed symmetries. However, for the graphical representation of the results it is advantageous to average the densities and velocity fields over the angle in order to reduce the statistical noise due to the finite number of test particles.

Let us start with the ground state density distributions shown in Fig. 1. Within the TF approximation, the ground states of all nuclei are spherical. Therefore, the ground state densities  $\tilde{\rho}$  were averaged over the full solid angle. In terms of the test-particle positions  $\mathbf{r}_i$ , the angle-averaged densities can be expressed as

$$\tilde{\rho}(r) = \sum_{i=1}^{NA} \frac{e^{-(r-r_i)^2/d^2} - e^{-(r+r_i)^2/d^2}}{\mathcal{N}4\pi^{3/2}rr_id}. \quad (\text{A1})$$

The dipole excitations considered in this work destroy the spherical symmetry, but not the cylindrical symmetry with respect to the  $z$  axis. In Figs. 5-7 and 9-14, this symmetry was used to reduce the statistical fluctuations by averaging the density  $\tilde{\rho}$  and the components  $\tilde{j}_\perp$  and  $\tilde{j}_z$  of the current density over the azimuthal angle  $\phi$  ( $\tilde{j}_\phi = 0$  for the excitation operators under consideration). After this averaging, the final expressions for  $\tilde{\rho}$  and  $\tilde{\mathbf{j}}$  in terms of the test particle positions  $\mathbf{r}_i$  and momenta  $\mathbf{p}_i$  read:

$$\tilde{\rho}(r_\perp, z) = \sum_{i=1}^{NA} \frac{e^{-\frac{(z-z_i)^2 + r_\perp^2 + r_{\perp i}^2}{d^2}}}{\mathcal{N}(\sqrt{\pi}d)^3} I_0\left(\frac{2r_\perp r_{\perp i}}{d^2}\right), \quad (\text{A2})$$

$$\tilde{j}_z(r_\perp, z) = \sum_{i=1}^{NA} p_{zi} \frac{e^{-\frac{(z-z_i)^2 + r_\perp^2 + r_{\perp i}^2}{d^2}}}{\mathcal{N}(\sqrt{\pi}d)^3} I_0\left(\frac{2r_\perp r_{\perp i}}{d^2}\right), \quad (\text{A3})$$

$$\tilde{j}_\perp(r_\perp, z) = \sum_{i=1}^{NA} p_{\perp i} \cos \phi_{r_i p_i} \frac{e^{-\frac{(z-z_i)^2 + r_\perp^2 + r_{\perp i}^2}{d^2}}}{\mathcal{N}(\sqrt{\pi}d)^3} I_1\left(\frac{2r_\perp r_{\perp i}}{d^2}\right), \quad (\text{A4})$$

where  $I_0$  and  $I_1$  are modified Bessel functions [35] and  $\phi_{r_i p_i}$  is the difference of the azimuthal angles of  $\mathbf{r}_i$  and  $\mathbf{p}_i$ , i.e.,

$$p_{\perp i} \cos \phi_{r_i p_i} = \frac{x_i p_{xi} + y_i p_{yi}}{\sqrt{x_i^2 + y_i^2}}. \quad (\text{A5})$$

### Appendix B: Transition probabilities and energy weighted sum rule

Often, the  $B(E1)$  value of the pygmy mode or its contribution to the EWSR are used as a measure for the strength of the pygmy mode. According to the definitions given in Ref. [28], the reduced transition probability  $B(E1; 0 \rightarrow 1)$  from the  $I_1 = 0$  ground state to a  $I_2 = 1$  excited state can be related to the strength function  $S(E)$  corresponding to the electric dipole operator (27) as follows:

$$\frac{dB(E1; 0 \rightarrow 1)}{dE} = \frac{9e^2}{4\pi} S(E). \quad (\text{B1})$$

Since the BCP functional does not introduce an effective mass ( $m^* = m$ ), the EWSR (Thomas-Reiche-Kuhn sum rule)

$$\int_0^\infty dE E S(E) = \frac{\hbar^2}{2m} \frac{NZ}{A}. \quad (\text{B2})$$

should be exactly fulfilled. In the numerical results discussed in Sec. III A, the deviation from the exact result is less than 1%.



- 
- [1] N. Paar, D. Vretenar, E. Khan, and G. Colò, Rep. Prog. Phys. **70** (2007), 691.
  - [2] S. Goriely, Phys. Lett. B **436**, 10 (1998).
  - [3] R. Mohan, M. Danos, and L.C. Biedenharn, Phys. Rev. C **3**, 1740 (1971).
  - [4] Y. Suzuki, K. Ikeda, and H. Sato, Prog. Theor. Phys. **83**, 180 (1990).
  - [5] F. Catara, E.G. Lanza, M.A. Nagarajan, and A. Vitturi, Nucl. Phys. A **624**, 449 (1997).
  - [6] D. Vretenar, N. Paar, P. Ring, and G.A. Lalazissis, Nucl. Phys. A **692**, 496 (2001).
  - [7] D. Peña Arteaga, E. Khan, and P. Ring, Phys. Rev. C **79**, 034311 (2009).
  - [8] N. Ryezayeva *et al.*, Phys. Rev. Lett. **89**, 272502 (2002).
  - [9] N. Tsoneva and H. Lenske, Phys. Rev. C **77**, 024321 (2008).
  - [10] S.F. Semenko, Sov. J. Nucl. Phys. **34**, 356 (1981).
  - [11] E.B. Balbutsev and I.N. Mikhailov, J. Phys. G **14**, 545 (1988); E.B. Balbutsev, I.V. Molodtsova, and A.V. Unzhakova, Europhys. Lett. **26**, 499 (1994).
  - [12] S.I. Bastrukov, S. Misicu, and A.V. Sushkov, Nucl. Phys. A **562**, 191 (1993).
  - [13] D. Vretenar, N. Paar, P. Ring, and T. Nikšić, Phys. Rev. C **65**, 021301(R) (2002).
  - [14] H. Steinwedel and J.H.D. Jensen, Phys. Rev. **79**, 1019 (1950).
  - [15] P. Ring and P. Schuck, *The Nuclear Many-Body Problem* (Springer, New York, 1980).
  - [16] D.M. Brink, A. Dellafore, and M. Di Toro, Nucl. Phys. A **456**, 205 (1986).
  - [17] G.F. Burgio and M. Di Toro, Nucl. Phys. A **476**, 189 (1988).
  - [18] G.F. Bertsch et S. Das Gupta, Phys. Rep. **160**, 189 (1988).
  - [19] T. Gaitanos, A. B. Larionov, H. Lenske, and U. Mosel, Phys. Rev. C **81**, 054316 (2010).
  - [20] M. Baldo, P. Schuck, and X. Viñas, Phys. Lett. B **663**, 390 (2008).
  - [21] W. Botermans and R. Malfliet, Phys. Rep. **198**, 115 (1990).
  - [22] C. Grégoire, B. Remaud, F. Sébille, L. Vinet, and Y. Raffray, Nucl. Phys. A **465**, 317 (1987).
  - [23] T. Fennel, G.F. Bertsch, and K.-H. Meiwes-Broer, Eur. Phys. J. D **29**, 367 (2004).
  - [24] J. Aichelin, Phys. Rep. **202**, 233 (1991).
  - [25] W.C. Swope, H.C. Andersen, P.H. Berens, and K.R. Wilson, J. Chem. Phys. **76**, 637 (1982).
  - [26] L. Robledo, talk given at the conference “Many-body correlations from dilute to dense nuclear systems”, February 15-18, 2011, Paris, France.
  - [27] A.L. Fetter and J.D. Walecka, *Quantum Theory of Many-Particle Systems* (McGraw-Hill, New York, 1971).
  - [28] A. Bohr and B.R. Mottelson, *Nuclear Structure. Vol. 1: Single-Particle Motion* (Benjamin, New York, 1969).
  - [29] S.C. Fultz *et al.*, Phys. Rev. **186**, 1255 (1969).
  - [30] G.F. Bertsch, P.F. Bortignon, and R.A. Broglia, Rev. Mod. Phys. **55**, 287 (1983).
  - [31] P. Adrich *et al.*, Phys. Rev. Lett. **95**, 132501 (2005).
  - [32] A. Leistenschneider et al., Phys. Rev. Lett. **86**, 5442 (2001).
  - [33] P. Papakonstantinou, V.Yu. Ponomarev, R. Roth, and J. Wambach, Eur. Phys. J. A **47**, 14 (2011).
  - [34] S.I. Bastrukov, I.V. Molodtsova, D.V. Podgany, Ş. Mişicu, and H.-K. Chang, Phys. Lett. B **664**, 258 (2008).
  - [35] M. Abramowitz and I.A. Stegun, *Handbook of Mathematical Functions* (Dover, New York, 1965).